

Modification of Mesoporous LiMn_2O_4 and $\text{LiMn}_{2-x}\text{Co}_x\text{O}_4$ by SILAR Method for Highly Efficient Water Oxidation Electrocatalysis

Irmak Karakaya, Ferdi Karadas, Burak Ulgut, and Ömer Dag*

Iridium, ruthenium, and cobalt oxides are target materials as efficient and stable mesoporous metal oxide electrocatalysts for oxygen evolution reaction (OER). However, they are costly, toxic, and not practical for an efficient OER process. Here, a two-step method is introduced, based on earth-abundant manganese; molten salt-assisted self-assembly process to prepare mesoporous $\text{LiMn}_{2-x}\text{Co}_x\text{O}_4$ ($x = 0-0.5$) modified electrodes, in which a systematic incorporation of Co(II) into the structure is performed using successive ionic layer adsorption and reaction followed by an annealing (SILAR-AN) process. Applying SILAR-AN over a stable $m\text{-LiMn}_{1.6}\text{Co}_{0.4}\text{O}_4$ electrode improves the OER performance; the Tafel slope and overpotential drop from 66 to 46 mV dec^{-1} and 304 to 265 mV (at 1.0 mA cm^{-2}), respectively. The performance of the modified electrodes is comparable to benchmark IrO_2 and RuO_2 catalysts and much better than cobalt oxide electrodes. Electronic interactions between the neighboring Mn and Co sites synergistically amplify the OER performance of the $m\text{-LiMn}_{2-x}\text{Co}_x\text{O}_4$ electrodes. The data are compatible with an eight steps nucleophilic acid-base reaction mechanism during OER.

in recent years.^[6-11] However, cobalt is a toxic, and relatively low abundant element that needs to be changed with a more abundant and less toxic element, such as manganese. Manganese oxides and mixed oxides have also been investigated that displayed a lower OER efficiency and lower stability.^[12-17] Most studies show that the cobalt is a key element for an efficient OER such that incorporation of cobalt into manganese oxide lattice improves the OER efficiency and stability of a modified electrode.^[17]


Mesoporous metal oxides have been targeted as efficient electrocatalysts for the OER. Several synthetic protocols, including hard and soft templating methods have been developed to produce mesoporous metal oxides.^[21-27] Hard templating method typically uses ordered mesoporous silica or carbon as a mold to produce ordered mesoporous metal oxide powders.^[24,25] Soft templating methods, such as evaporation induced self-assembly^[23] and molten salt assisted self-assembly (MASA)^[24-27] processes, have been developed for the fabrication of mesoporous metal oxide thin films that would be more practical in an electrochemical process. The MASA process is a more applicable method to produce disordered mesoporous transition metal oxides of metals that do not have alkoxide precursors; the metal precursors used in this process are usually metal nitrate, metal acetate, or metal chloride salts.^[24-27] In the MASA process, a transition metal salt that has low melting point (such as first row transition metal nitrates) or high solubility (such as most lithium salts) could be used as a solvent to assemble surfactant molecules into a lyotropic liquid crystalline mesophase.^[28-31] Salt is in a molten phase in the mesophase (confined nanospace in hydrophilic domains) due to nanospace effect (NE).^[30] The NE, not only reduces the melting point of the salts,^[30] also enhances the solubility of the salts.^[31] Moreover, presence of two salts (lithium and transition metal salts) creates a synergistic effect that further improves the stability and high salt uptake of the salt-surfactant mesophases. Coating of a mesophase as a thin film and its calcination at elevated temperatures produce mesoporous metal oxide thin films.^[26-38] The MASA process has already been employed to two groups of metal oxides. In the first group, a silica or titania precursor is used as a polymerizing agent at room temperature together with a transition metal nitrate salt to produce

1. Introduction

Oxygen evolution reaction (OER) electrocatalysts are important group of materials that may replace currently used expensive platinum electrodes. Transition metal oxides and metal sulfides with high surface area are the target materials in the literature.^[1-20] Although IrO_2 and RuO_2 -based electrodes are the benchmark catalytic systems, they are precious metals, which limits their applications in scalable devices.^[3-5] 3d metal oxides, particularly cobalt oxides can be considered as alternative class of catalysts for the OER process.^[6-11] For an efficient OER, porous cobalt oxides have been extensively investigated

I. Karakaya, Prof. F. Karadas, Prof. B. Ulgut, Prof. Ö. Dag
Department of Chemistry
Bilkent University
Ankara 06800, Turkey
E-mail: dag@fen.bilkent.edu.tr

Prof. F. Karadas, Prof. B. Ulgut, Prof. Ö. Dag
UNAM – National Nanotechnology Research Center and Institute of
Materials Science and Nanotechnology
Bilkent University
Ankara 06800, Turkey

 The ORCID identification number(s) for the author(s) of this article can be found under <https://doi.org/10.1002/admt.202000353>.

DOI: 10.1002/admt.202000353

mesoporous silica-metal oxides (such as CdO/SiO₂ and ZnO/SiO₂)^[26] or metal titanates (such as MnTiO₃, CoTiO₃, CdTiO₃, Zn₂TiO₄, and Li₅Ti₄O₁₂).^[27,28] In the second group, a clear salt(s) and nonionic/cationic surfactants solution is coated to produce a stable thin film of an lyotropic liquid crystalline (LLC) mesophase. Aging the mesophase at room temperature (RT) does not alter the stability or structure. Moreover, calcination of the LLC phase produces the mesoporous metal oxide film of the salt; the mesoporous LiMn_{2-x}Co_xO₄, LiCoO₂, and NiO thin films have recently been synthesized as a second group of metal oxides.^[17,24,25]

Successive ionic layer adsorption and reaction (SILAR) method has also been an effective method to modify porous materials^[32] either growing special coatings layer by layer or quantitatively introducing/controlling dopant(s) over surfaces to alter, protect, and/or functionalize the surface of the modified materials.^[33–35] Furthermore, the SILAR method has been employed to coat electrode surfaces by another compound(s) to either change the surface properties or to protect the surface in an electrochemical process. A multilayered material could be fabricated by SILAR that is followed by an annealing step (SILAR-AN) or a chemical reaction (SILAR-CR). For instance, in quantum dot sensitized solar cell, the SILAR-CR method has been successfully employed to slow/stop reduction reaction (counter-reaction) on the anode surface in a quantum dot sensitized solar cells.^[34] SILAR-CR and SILAR-AN are simple and effective methods to adsorb ions over a material surface for a further reaction or thermal treatment, respectively, to coat an atomically thin layer(s) of active and/or protective species over the thin films and also to produce core–shell nanoparticles as electrodes for various applications.^[32–35]

Here, we employed both MASA and SILAR-AN methods to produce mesoporous LiMn_{2-x}Co_xO₄ thin films as an efficient electrocatalyst for OER with relatively low cobalt content. The MASA and SILAR-AN methods were employed to produce stable mesoporous thin films of cobalt enriched LiMn_{2-x}Co_xO₄ ($x = 0–0.5$) electrodes that have excellent stability and high efficiency in the OER in an alkali media. The motivation of this work is to improve the stability and efficiency of manganese (less toxic and more abundant) rich mesoporous LiMn_{2-x}Co_xO₄ electrodes for OER processes.

2. Results and Discussion

2.1. Synthesis and Characterization of Mesoporous LiMn_{2-x}Co_xO₄ Electrodes

In the fabrication of mesoporous LiMn_{2-x}Co_xO₂ (m-LiMn_{2-x}Co_xO₄) electrodes and their modifications using a small amount of cobalt have been carried by using two different synthesis protocols. In the first protocol, a previously established MASA^[17] process has been employed to produce the thin film electrodes over the fluoride doped thin oxide (FTO)-coated glass substrates (m-LiMn_{2-x}Co_xO₄). Simply, a clear MASA solution (LiNO₃, [Mn(H₂O)₄](NO₃)₂, [Co(H₂O)₆](NO₃)₂, P123, CTAB, HNO₃ and ethanol) was spin-coated over FTO-coated glass and calcined at 300 °C to obtain the thin-film electrode (denoted as m-LiMn_{2-x}Co_xO₄), see ref. [17] for details. SILAR-AN has been

employed multiple times to modify those electrodes (denoted as m-LiMn_{2-x}Co_xO₄-#) in the second protocol.

The cobalt-free m-LiMn₂O₄ electrode has a typical Burrett–Emmett–Teller (BET) surface area of 98 m² g⁻¹. The BET surface area gradually increases up to 144 m² g⁻¹ with increasing cobalt in the m-LiMn_{2-x}Co_xO₄ sample (x is 0.5). Also note that further increasing cobalt reduces the surface to 124 and 103 m² g⁻¹, as recorded from m-LiMnCoO₄ and m-LiMn_{0.5}Co_{1.5}O₄, respectively.^[17] The increase in the surface area in the presence of two salts could be related to synergic effects of two molten salts in the LLC media. Note that while one salt-surfactant mesophases have limited stability against salt leach out; presence of a second even a third salt stabilizes the salt-surfactant LLC mesophase at much higher salt concentrations.^[36] Furthermore, it has been previously shown that the pore-walls are nanocrystalline at all compositions with a typical crystallite size of 5–6 nm (as predicted from Scherrer's equation using X-ray diffraction (XRD) data, transmission electron microscopy (TEM) images).^[17] However, the surface area of the films gradually decreases with increasing calcination/annealing temperature; such as it is 90, 69, and 33 m² g⁻¹ at 400, 500, and 600 °C, respectively, in the m-LiMn₂O₄.^[17] The electrochemical behaviors and water oxidation electrocatalytic performance of these electrodes have also been investigated in our previous work using m-LiMn_{2-x}Co_xO₄ electrodes, where x is 0, 0.5, 1.0, 1.5, and 2.^[17] The m-LiMn₂O₄ electrode has a high Tafel slope (130 mV dec⁻¹) and high overpotential (417 mV at 1 mA cm⁻² and 541 mV at 10 mA cm⁻²) and low stability during chronopotentiometry (CP) experiments in 1 M KOH solution. However, introducing a 25 mole% cobalt (m-LiMn_{1.5}Co_{0.5}O₄) improved the electrocatalytic performance (such as the Tafel slope dropped to 66 mV dec⁻¹ with overpotentials of 300 and 367 mV at 1 and 10 mA cm⁻² current densities, respectively, after IR compensation^[17]) and the stability of the m-LiMn_{1.5}Co_{0.5}O₄ electrode. In higher cobalt-containing electrodes (m-LiMn_{2-x}Co_xO₄, where x is larger than 0.5), these values slightly improved up to 64 mV dec⁻¹ for the Tafel slope and 280 and 345 mV at 1 and 10 mA cm⁻², respectively, for the overpotentials in the m-LiMnCoO₄ electrode.^[17] Extra overpotentials add up to these values at higher current densities due to the electrode resistance that mostly originates from FTO.^[17] The typical resistance of the electrode on FTO varies from 15 to 20 Ω and adds extra 150–200 mV at 10 mA cm⁻² and 1.5–2.0 V at 100 mA cm⁻² current densities, see Figure S1a (Supporting Information). Replacing FTO with a graphite substrate (0.7 mm diameter pencil tips, which are pressed graphite, calcined at 300 °C, prior to use) improves the overpotential values at high current densities. The overpotential drops from 1277 to 523 mV at 60 mA cm⁻² by simply using a better conducting substrate, such as graphite, see Figure S1b (Supporting Information). The overpotential versus current density plot of the graphite coated m-LiMnCoO₄ electrode is also linear with a slope of 3.77 Ω. The origin of these losses is mostly from IR drop due to electrode resistance. The estimated overpotential in the graphite coated electrode at 60 mA cm⁻² current density (from the Tafel equation, $\eta = a + b \log(j)$, where η is overpotential, b is the Tafel slope, and j is the current density) is around 398 mV but the observed value is 523 mV. The resistance of the graphite-coated electrode is estimated to be around 2.08 Ω (calculated from

Ohm's law (523–398) mV 60 mA⁻¹). The same calculation gives an FTO-coated electrode resistance of 177 Ω (1.460–398)/60, however, the resistance that can be evaluated from the overpotential versus current density plot is 19.01 Ω, see Figure S1 (Supporting Information). The difference is remarkably similar, 1.69 (=3.77–2.08) and 1.31 (=19.01–17.7) Ω in both graphite- and FTO-coated electrodes, respectively, and must be related to the rate of OER over these two electrodes. The major limitation of the m-LiMn_{2-x}Co_xO₄ electrodes in the OER originates from highly resistive substrates. The potential losses at high current densities are purely ohmic.

Besides the conductivity advantage of graphite, there are also some disadvantages to using graphite as a substrate in terms of fabricating the electrodes. It is more difficult to control the thickness/amount of m-LiMn_{2-x}Co_xO₄ films by dip-coating graphite rods using clear homogeneous MASA solutions, but this problem could be overcome by using graphite-plates. Moreover, the dip-coating method produces nonuniform film thickness and is usually employed to prepare thicker films that may elevate the OER performance (more electrocatalyst) but increasing the thickness of the electrode will also increase the electrode resistance that will lower the EOR performance at high current densities. To overcome these issues and be able to compare the results from both substrates, the graphite electrodes were coated by using 10 times diluter MASA solutions; dilution also ensures a thinner film over the graphite surface. The cyclic voltammetry (CVs) of FTO- and graphite-coated electrodes (Figure S1, Supporting Information) clearly show that the graphite-coated electrode is even thinner than the FTO-coated electrode as evidenced by lower current density in the oxidation/reduction peaks from the electrode surface of the graphite-coated electrode, see Figure S1a (Supporting Information). Overall, a better conducting substrate is more beneficial for its use in practical applications.

In this investigation, we took the electrodes with modest cobalt content (such as m-LiMn₂O₄, m-LiMn_{1.5}Co_{0.5}O₄, m-LiMn_{1.8}Co_{0.2}O₄, m-LiMn_{1.7}Co_{0.3}O₄, and m-LiMn_{1.6}Co_{0.4}O₄ electrodes) with decent stability in the alkaline media and improve their electrocatalytic performance and stability by employing SILAR-AN method. All the measurements were carried out using the electrodes prepared over the FTO surface to be able to compare the electrodes with each other. Note also that all the thin-film electrodes (m-LiMn_{2-x}Co_xO₄ (x = 0–0.5)) over the FTO electrodes weigh around 0.1 mg with a typical thickness of around 400 nm.

Figure 1 shows a schematic representation of the SILAR-AN (modification) process. First, m-LiMn₂O₄ electrode was modified to obtain 4 new m-LiMn₂O₄-# (# is the number of SILAR-AN employed and is 1, 3, 5, and 7) electrodes and characterized by using XRD technique. In each coating, the SILAR coating

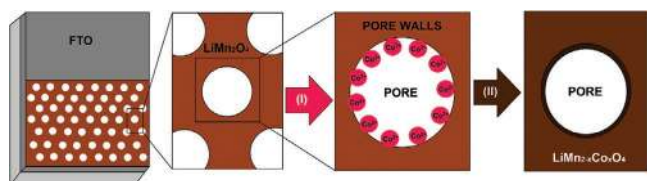


Figure 1. Schematic representation of the SILAR-AN process: (I) Dipping into 1 M Co²⁺ solution and washing and (II) annealing.

was followed by a good washing and annealing/calcination process at 300 °C before going to the next coating or using as an electrode to ensure homogeneous cobalt coatings. Figure 2 shows a series of powder X-ray diffraction (PXRD) patterns of the modified samples together with reference data of bulk LiMn₂O₄, LiCoO₂, and Co₃O₄ to identify whether the cobalt ions diffuse into pore-walls or it deposits as a thin layer of cobalt oxide over the pore-walls. The PXRD patterns of the m-LiMn₂O₄ (it can be indexed to spinel structure) and their modified versions (m-LiMn₂O₄-#, where # is 1, 3, 5, and 7) are remarkably similar. However, all the diffraction lines slightly shift to higher angles, maybe indicating a homogeneous mixing (solid-solution) of cobalt into the m-LiMn₂O₄ spinel structure, see Figure 2b. The XRD patterns were compared with the PDF cards of possible products, Co₃O₄ (PDF 00-042-1467) and LiCoO₂ (PDF 00-044-0145) to shed light on how the annealing proceeds. However, the PDF cards of Co₃O₄, LiCoO₂, and m-LiMn_{2-x}Co_xO₄ are very similar to each other, therefore it is difficult to determine whether the cobalt is forming its oxide or reacting with the m-LiMn₂O₄ to form m-LiMn_{2-x}Co_xO₄ from the XRD data, see Figure 2. Employing the SILAR-AN process multiple times and further annealing the samples at higher temperature provide extra but weaker diffraction lines that can be indexed to crystalline Mn₃O₄ nanoparticles (PDF-00-024-0734 card of bulk Mn₃O₄). It means that cobalt species over the pore-wall surface diffuse into the m-LiMn₂O₄ pore-walls and undergo an exchange reaction with manganese ions that, with further heating, form its own oxide phase (Mn₃O₄) over the pore-walls and likely on top of the film/electrode surface, see latter.

We also recorded high-resolution X-ray photoelectron spectroscopy (XPS) data of the electrodes (over the FTO glass, top electrode surface) and their grind powders (obtained by scraping the electrode and grinding) of the m-LiMn₂O₄-# (# = 0, 1, 3, 5, and 7) and m-LiMn_{2-x}Co_xO₄, see Figure 3; and Figures S2–S4 (Supporting Information), in the O 1s, Co 2p, and Mn 2p regions. The spectrum of m-LiMn₂O₄ in the Mn 2p (²P_{3/2}) region consist of a peak at 643 eV due to Mn⁴⁺ sites with a shoulder on the low energy side due to Mn³⁺ sites, characteristic for spinel LiMn₂O₄.^[37] The Mn 2p spectrum of the m-LiMn_{1.5}Co_{0.5}O₄ film is very similar to m-LiMn₂O₄, indicating a solid solution formation in the m-LiMn_{1.5}Co_{0.5}O₄ in terms of Mn³⁺/Mn⁴⁺ sites in the structure. With increasing cobalt in the m-LiMn₂O₄ sample, the Mn 2p (²P_{3/2}) peaks gradually shift to a lower binding energy, indicating the presence/formation of Mn species with a lower oxidation state in the

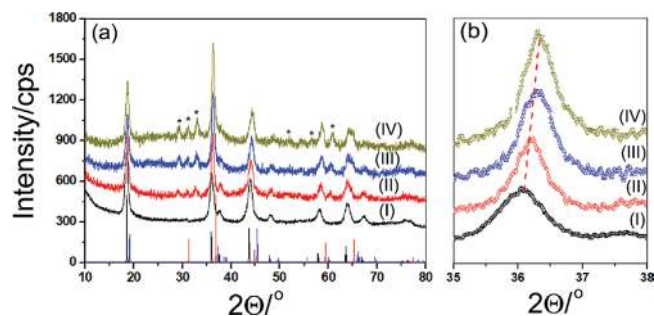


Figure 2. PXRD patterns of m-LiMn₂O₄-# a,b), where # is (I) 0, (II) 1, (III) 3, and (IV) 5 (the reference data in panel a): black lines-LiMn₂O₄, blue lines-LiCoO₂, red lines-Co₃O₄, and *-Mn₃O₄.

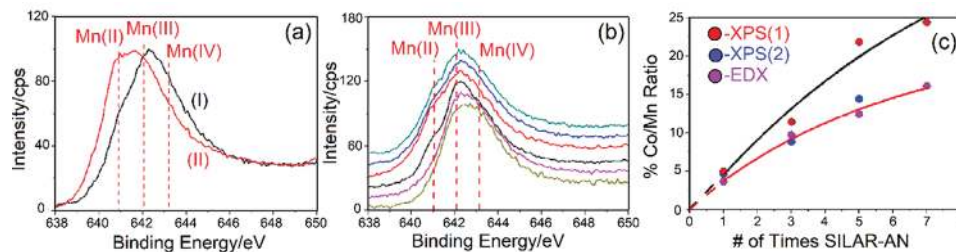


Figure 3. Mn 2p XPS spectra of: a) grind sample of $m\text{-LiMn}_2\text{O}_4\text{-3}$ (I) and the electrode top surface (II), b) bottom to top: $m\text{-LiMnCoO}_4$ (olive), $m\text{-LiMn}_{1.5}\text{Co}_{0.4}\text{O}_4$ (pink), and $m\text{-LiMn}_2\text{O}_4\text{-}\#$ ($\#$ is 0 (black), 1 (red), 3 (blue), and 5 (green)), and c) percent Co/Mn from XPS (electrode surface, XPS(1) and grind sample XPS(2), and EDX data.

modified samples. The difference spectrum of the $m\text{-LiMn}_2\text{O}_4$ and modified $\text{LiMn}_2\text{O}_4\text{-}\#$ clearly shows that the intensity of the low energy side of the main $2\text{P}_{3/2}$ peak increases and the high energy side decrease (see Figure S3a, Supporting Information), supporting the above statement. The line shape in the Mn $2\text{P}_{3/2}$ region closely resembles the spectrum of Mn_3O_4 ^[38] (see Figure S2c, Supporting Information). Both XRD and XPS data collectively show the formation and accumulation of Mn_3O_4 particles over the electrode surface. We also collected energy dispersive X-ray (EDX) data of these samples and found out that the cobalt amount in the samples gradually increases with multiple coatings, the cobalt amount increases from 3.5 mole% in the $\text{LiMn}_2\text{O}_4\text{-1}$ –16 mole% in the $\text{LiMn}_2\text{O}_4\text{-7}$ film, see Figure S5a,b (Supporting Information). The plot of the relative amount of cobalt deposited with respect to the number of coating gradually increases and converges to a value around 22 mole%, see Figure S5b (Supporting Information).

The surface area was also measured and calculated using N_2 adsorption–desorption isotherms and BET method, see Figure S6 and Table S1 (Supporting Information). Like the elemental analysis, the surface area calculated from the BET equation drops by 30% after the 7th coating. Notice also that there is sharp surface area drop (from 98 to $75\text{ m}^2\text{ g}^{-1}$), a larger pore (from 12.8 to 21.3 nm, calculated from Barrett–Joyner–Halenda equation using desorption isotherm) and pore volume expansions (from 0.32 to $0.43\text{ cm}^3\text{ g}^{-1}$) in the first coating, however, further coatings dropped the BET surface area, changed the pore size and pore volume in less extend (see Table S1, Supporting Information). The data show that SILAR-AN coating is uniform and applicable to modify existing mesoporous materials.

Scanning electron microscopy (SEM) images of the $m\text{-LiMn}_2\text{O}_4$ and modified $m\text{-LiMn}_2\text{O}_4\text{-}\#$ films were also recorded to elucidate the details of surface morphology. Surface morphology of the films is unaltered up to 3rd coating, but individual nanoparticles appear in 5th coating and dominate over the surface with further coatings, see Figure S6 (Supporting Information).

XPS data were further analyzed to elucidate the compositional and morphologic changes in the internal and external surface of the electrodes by increasing cobalt content by employing SILAR-AN modification and MASA methods. The O 1s region displays multiple features at 529.9 (a peak) and 531.2 eV (a shoulder) tailing down to 533 eV that show drastic changes with increasing cobalt loading over the electrode top surface, see Figure S2a (Supporting Information). As shown

in Figure S2a (Supporting Information), the shoulder at 531.2 eV gradually increases up to 5th loading. The peak at 529.9 eV (peak I) is due to lattice oxygens and the other features at 530.7 (peak II), 531.2 (peak III), and 532.3 eV (peak IV) have been assigned to hydroxy, peroxy, and coordinated water oxygens,^[39,40] respectively, see Figures S2a, S3b, and S4 (Supporting Information). With cobalt loading, while the Co 2p region shows no response other than a gradual increase in intensity, the O 1s peaks follow the trend in Mn 2p region. The signals in the Co 2p ($2\text{P}_{3/2}$) region are relatively weaker and broader in the spectra of the electrode surface (see Figure S2b (Supporting Information)). The Co 2p spectra of the modified $m\text{-LiMn}_2\text{O}_4$ electrodes display a broad peak at 780.2 eV with a satellite peak at 786 eV. However, the spectrum of the grind samples displays a relatively sharper peak at around 780.5 eV with a satellite peak at 790 eV, see Figure S2c (Supporting Information). The satellite peak of Co(II) species appears at 786 eV and Co(III) and Co(IV) species at 790 eV.^[41] As shown, the main $2\text{P}_{3/2}$ peak is not very sensitive to the oxidation state of the cobalt species, the satellite peaks are very sensitive and commonly used to identify the oxidation state of cobalt species.^[41] Therefore, it is reasonable to suggest that while the electrode surface is rich with Co(II) species, the interior surface is modified by Co(III) and/or Co(IV) species in the SILAR-AN process. Moreover, the Co 2p spectra of all grind samples are like $m\text{-LiMn}_{2-x}\text{Co}_x\text{O}_4$. This concludes that Co incorporates into $m\text{-LiMn}_2\text{O}_4$ and produces $m\text{-LiMn}_{2-x}\text{Co}_x\text{O}_4$ on the pore-walls. However, there is some accumulation of Co(II) species over the electrode surface. This is also clearly visible in the % Co/Mn versus number of loading plots in Figure 3c, see later.

Figure 3a compares the Mn 2p ($2\text{P}_{3/2}$) region of the electrode surface and grid powder upon 3 consecutive SILAR-AN processes. The shoulder on the low energy side (due to Mn^{2+} species) becomes the most intense peak in the spectra of the electrode surfaces (Figure S2c, Supporting Information) while the scraped and grind powder samples display no change (see Figure 3b) with multiple loading. The top surface of the $m\text{-LiMn}_2\text{O}_4\text{-3}$ and $m\text{-LiMn}_2\text{O}_4\text{-5}$ electrodes have similar spectra, see Figure S2d (Supporting Information), supporting our above proposal. The amount of Mn^{2+} species is more over the electrode surface, indicating that crystalline Mn_3O_4 (Mn(II) $\text{Mn(III)}_2\text{O}_4$) species are accumulating over the electrode surface, see Figure 3a.

As a result of these observations, we suggest the following redox reactions (see Equations (1) and (2)) between the Co(II) ions on the surface and $m\text{-LiMn}_2\text{O}_4$ during the modification

process to alter the electrode internal and external surface. Comparison of all the XPS data suggest that after 5th loading, the small pores get plugged (as also observed in the N_2 adsorption–desorption isotherms) by the out coming manganese species (likely Mn_3O_4 nanoparticles) that accumulate over the electrode surface and no more appreciable loading is possible after 5th loading

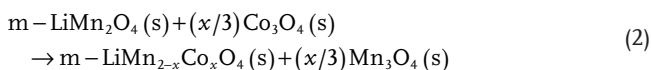
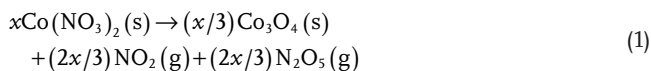


Figure 3c shows 3 plots obtained from the XPS of grind powers and electrodes surface and EDX data. Clearly EDX data show the bulk composition of the samples. However, the XPS data provide compositional information of the top few layers of the material. The plot of percent Co/Mn versus the number of SILAR-AN of both XPS and EDX of data of the grind samples overlap with each other. Therefore, the XPS data of the grind samples provide more information about the internal surface of the electrodes, while the XPS of the electrode surface provides information on the top surface of the electrodes. Both XPS and EDX data of the grind samples collectively show that the SILAR-AN is an effective method to homogeneously coat the internal surface of the $m-LiMn_{2-x}Co_xO_4$ thin films. The plot of %Co/Mn from XPS data of the electrode surface linearly increases with the increasing number of SILAR-AN process. Therefore, the electrode surface becomes richer with Mn(II) and Co(II) species with further coatings.

Further analysis of the O 1s spectra of the electrodes and ground powders provide some insightful information on the surface composition of the internal versus external surface of the electrodes, see Figures S2a and S3b (Supporting Information). The peaks due to peroxide (M–OOH) and hydroxide (M–OH) species increase with an increasing number of applied SILAR-AN over the top surface of the electrodes (see Figure S2a, Supporting Information). However, this is not the case on the internal surface of the electrodes; there is almost no change in the oxygen composition by increasing the number of loading in the interior of the electrodes. Figure S4 (Supporting Information) also displays O 1s spectra of 3 $m-LiMn_{2-x}Co_xO_4$ unmodified grind samples. Clearly, with increasing Co in the $m-LiMn_{2-x}Co_xO_4$ grind powder, the surface hydroxy, peroxy, water species increases. The modified electrodes are rich with hydroxy and peroxy species, while the unmodified ones are rich with water. It is reasonable to conclude that increasing cobalt at the surface and/or in the pore-walls increases the surface concentration of highly reactive hydroxide and peroxide species for the oxygen evolution reaction, see later. Moreover, the SILAR-AN modification enhances the formation of Mn_3O_4 over the electrode surface, the cobalt preferentially modifies and enhances the cobalt amount in the pore-walls. Therefore, the top surface of the pore-walls (interior surface) has cobalt rich Mn–Co oxide, hydroxide, peroxide, and water surface species that are collectively involved in the catalysis of water oxidation process, see later.

2.2. Electrochemical Behaviors of the $m-LiMn_{2-x}Co_xO_4$ and $m-LiMn_{2-x}Co_xO_4$ -# Electrodes

Modification of the $m-LiMn_2O_4$ electrodes by SILAR-AN in multiple steps produces a cobalt rich pore surface in $m-LiMn_2O_4$ -# electrodes. To test the modified electrodes, a detailed electrochemical characterization has been carried by first recording CVs of each electrode and compared with the bare $m-LiMn_2O_4$ electrode with respect to OER efficiency. The CVs of the $m-LiMn_2O_4$, $m-LiMn_{1.5}Co_{0.5}O_4$, and $m-LiMnCoO_4$ electrodes in 1 M KOH solution are shown in Figure 4. The features in the forward scan in the -0.4 – 0.2 V region, have been assigned to oxidation of manganese from 3+ to 4+,^[42–44] and the peak, at around 0.57 V (becomes visible in the $m-LiMnCoO_4$ sample) corresponds to the oxidation of cobalt from 3+ to 4+.^[45] A sharp increase after 0.8 V is due to catalytic water oxidation process. The reduction cycle reverses these processes and an intense and broad oxygen reduction peak^[46] is observed at around -0.3 V, see Figure 4a.

Figure 4b displays the CVs of the modified $m-LiMn_2O_4$ -# electrodes. The manganese oxidation/reduction current density decreases with modification, while no significant change in the cobalt redox region is observed. More importantly, there is a change in the OER potential range with modification; kinetics of the process improves with increasing amounts of modification. The current density at 1 V reaches 20 mA cm^{-2} in $m-LiMn_2O_4$ -1 electrode, showing the effectiveness of the SILAR-AN process, see Figure S8 (Supporting Information). One would expect that each modification will improve the electrocatalytic activity due to increasing cobalt loading on the surface. However, the slope of the current density versus potential curve gradually declines by further increasing the number of loading in the $m-LiMn_2O_4$ -# electrodes, see Figure S8 (Supporting Information). Remember also that we previously established the formation of the Mn_3O_4 species on the surface with increasing the loading numbers. Contaminating/covering the surface with a less active Mn species and decreasing the surface area (also evidenced from the current density drop in the CVs, see Figure 4b) could be the origin of such decrease in the current density with further loading.

Tafel slopes were evaluated using each modified electrode, see Figure S9 (Supporting Information). The Tafel slopes and overpotentials were extracted from 6 h CP experiment at a current density of 1 mA cm^{-2} , see Table 1. There is a definite improvement on the Tafel slope in the $m-LiMn_2O_4$ -1 electrode (it decreases from 130 for the $m-LiMn_2O_4$ to 82 mV dec^{-1} for

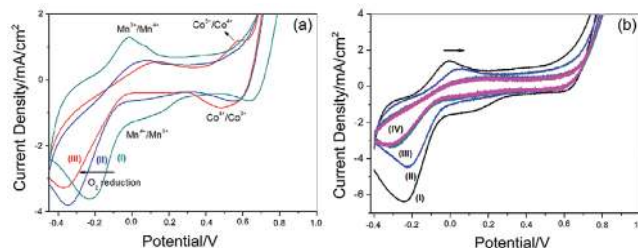


Figure 4. CVs of a) $m-LiMn_2O_4$ (I), $m-LiMn_{1.5}Co_{0.5}O_4$ (II), and $m-LiMnCoO_4$ (III) in 1 M KOH solution (x-axis was calibrated with respect to NHE) and b) modified electrodes ($m-LiMn_2O_4$ -# (# is 1 (I), 3 (II), 5 (III), and 7 (IV)).

Table 1. Tafel slopes and overpotentials at 1 mA cm⁻² of the m-LiMn₂O₄-# electrodes from 6 h CP experiments (*calculated at 300 °C, η-overpotentials).

Electrodes*	Tafel slope [mV dec ⁻¹]	η at 1 A cm ⁻² [mV]	Electrodes	Tafel slope [mV dec ⁻¹]	η at 1 mA cm ⁻² [mV]
m-LiMn ₂ O ₄	130	491	m-LiMn ₂ O ₄ -400	128	351
m-LiMn ₂ O ₄ -1	82	363	m-LiMn ₂ O ₄ -500	123	582
m-LiMn ₂ O ₄ -3	88	377	m-LiMn ₂ O ₄ -1-400	78	326
m-LiMn ₂ O ₄ -5	89	333	m-LiMn ₂ O ₄ -1-500	61	343
m-LiMn ₂ O ₄ -7	108	413			

the m-LiMn₂O₄-1 electrode), but further coating/loading gradually increases the Tafel slope up to 108 mV dec⁻¹, recorded for the m-LiMn₂O₄-7 electrode. It is likely that the m-LiMn₂O₄-7 electrode surface is covered with Mn₃O₄ particles. Notice also that the overpotential values also follow the same trend, see Table 1. These results are consistent with our proposal, such that the surface becomes Mn₃O₄ enriched in further coatings.

Furthermore, the effects of calcination/annealing temperature and composition (m-LiMn_{2-x}Co_xO₄, x = 0.1–0.5) to the performance and long-term stability of the electrodes were also investigated. Increasing annealing temperature of m-LiMn₂O₄ improved the crystallinity, which leads to a decrease in the surface area from 90 to 69 and to 33 m² g⁻¹ upon annealing at 400, 500, and 600 °C, respectively. The CVs of the annealed electrodes are similar to each other, see Figure S10a (Supporting Information). The Tafel slope is improved from 130 to 128 and to 123 mV dec⁻¹ with increasing annealing temperature from 300 to 400 and to 500 °C, respectively, although the surface area dropped from 98 to 33 m² g⁻¹. The CP results show that the performance of the electrode prepared at 400 °C improved slightly upon annealing, see tabulated data in Table 1. Similarly, that of m-LiMn₂O₄-1 electrode, annealed at various temperatures (300, 400, and 500 °C), also improved, see Table 1. The CV curves were recorded before and after CP measurements at 1 and 10 mA cm⁻² current densities, see Figure S10 (Supporting Information), to check the stability of the electrodes during long-term CP experiments. We found that the m-LiMn₂O₄ and m-LiMn₂O₄-# electrodes are not stable under CP conditions; the current density in OER range almost disappeared, see Figure 5a. Therefore, increasing the annealing temperature slightly improved the overpotentials but the stability issue remained problem in the m-LiMn₂O₄-# electrodes.

Since the stability issues of the m-LiMn₂O₄-# electrodes could not be resolved by thermal process or modification, we also prepared a series of m-LiMn_{2-x}Co_xO₄ electrodes and used for further investigation toward the same goal. It has been pre-

viously shown that the m-LiMn_{1.5}Co_{0.5}O₄ electrode (25% Co) has a good performance and stability in the OER at alkaline conditions, see Figure 5b.^[17] To determine the ideal cobalt ratio, a set of electrodes were prepared by using 5–25% cobalt nitrate in the initial synthesis solutions and the fabricated electrodes were tested for their stability in OER process in alkaline media.

Figure S11 (Supporting Information) shows photographs of a set of m-LiMn_{2-x}Co_xO₄ (0.1 ≤ x ≤ 0.5) thin films, prepared over glass substrates. Increasing cobalt amount in the meso-phase (as a result in m-LiMn_{2-x}Co_xO₄ films) improves the surface smoothness and uniformity of the m-LiMn_{2-x}Co_xO₄ films, especially over 10% cobalt (m-LiMn_{1.8}Co_{0.2}O₄). SEM images also show that m-LiMn_{1.8}Co_{0.2}O₄ (corresponds to 10% Co) is on the border between a good quality and nonuniform fragile film, see Figure S12 (Supporting Information). Unstable films contain small particles over their surface and their broken edges (cracks) are not as smooth, like the m-LiMn₂O₄ film. However, the SEM images show smoother edges in the m-LiMn_{2-x}Co_xO₄ (x ≥ 0.3), see Figure S12 (Supporting Information). To further evaluate the relationship between the film quality and long-term stability of the electrodes in the OER process, the CVs after various experiments (CP experiments at 1 mA cm⁻² for 12 h and 10 mA cm⁻² for 6 h) were also recorded (Figure S13, Supporting Information). Tafel slopes and overpotentials are tabulated in Table 2.

Table 2. Tafel slopes and overpotential results of the m-LiMn_{2-x}Co_xO₄, m-LiMn_{1.6}Co_{0.4}O₄-#, and m-LiMn_{1.7}Co_{0.3}O₄-# electrodes at 1 and 10 mA.

Electrodes	Tafel slope [mV dec ⁻¹]	Overpotential at 1 mA cm ⁻² for 12 h [mV]	Overpotential at 10 mA cm ⁻² for 6 h [mV]
m-LiMn ₂ O ₄	130	491	1354
m-LiMn _{1.9} Co _{0.1} O ₄	115	704	1601
m-LiMn _{1.8} Co _{0.2} O ₄	72	441	1327
m-LiMn _{1.7} Co _{0.3} O ₄	65	361	1123
m-LiMn _{1.6} Co _{0.4} O ₄	64	304	826
m-LiMn _{1.5} Co _{0.5} O ₄	66	294	750
m-LiMn _{1.6} Co _{0.4} O ₄	64	304	826
m-LiMn _{1.6} Co _{0.4} O ₄ -1	56	325	657
m-LiMn _{1.6} Co _{0.4} O ₄ -3	55	279	576
m-LiMn _{1.6} Co _{0.4} O ₄ -5	53	265	546
m-LiMn _{1.7} Co _{0.3} O ₄	65	304	826
m-LiMn _{1.7} Co _{0.3} O ₄ -1	56	290	837
m-LiMn _{1.7} Co _{0.3} O ₄ -3	57	283	596
m-LiMn _{1.7} Co _{0.3} O ₄ -5	50	270	636

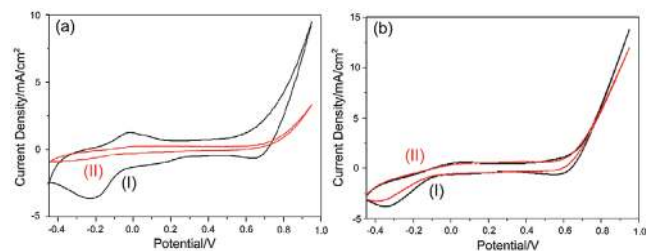


Figure 5. CVs of a) m-LiMn₂O₄ and b) m-LiMn_{1.5}Co_{0.5}O₄ before (I) and after (II) CP experiment (12 h at 1 mA cm⁻² and 6 h at 10 mA cm⁻², x-axis was calibrated with respect to NHE).

While the $m\text{-LiMn}_{1.9}\text{Co}_{0.1}\text{O}_4$ electrode (corresponds to a 5 mole% cobalt) has a high Tafel slope (115 mV dec^{-1}), like $m\text{-LiMn}_2\text{O}_4$, it incrementally decreases by increasing cobalt in the electrodes. Addition of another 5% cobalt ($m\text{-LiMn}_{1.8}\text{Co}_{0.2}\text{O}_4$ electrode) improves the efficiency of the electrode, providing a Tafel slope of 72 mV dec^{-1} . However, the Tafel slope is improved further with further addition of cobalt, up to 25%, see Table 2.

The CP experiments at 1 and 10 mA cm^{-2} using each electrode shows similar trends. The overpotential values (without IR compensation) improved from 491 to 294 mV at 1 mA cm^{-2} and 1354 to 750 mV at 10 mA cm^{-2} , going from $m\text{-LiMn}_2\text{O}_4$ to $m\text{-LiMn}_{1.5}\text{Co}_{0.5}\text{O}_4$ electrodes in 1 M KOH solution. The stability of the electrodes was also tested by recording their CVs after the CP experiments at 1 (12 h) and 10 mA cm^{-2} (6 h), see Figure S13b,c (Supporting Information). The CVs of the electrodes (with a 5–15 mole% cobalt) after 12 h CP at 1 mA cm^{-2} show a drastic current density decrease in the OER potential range. However, the drops in the CVs of the $m\text{-LiMn}_{1.6}\text{Co}_{0.4}\text{O}_4$ and $m\text{-LiMn}_{1.5}\text{Co}_{0.5}\text{O}_4$ electrodes are insignificant. This is because the electrodes with a lower cobalt amount, below 20 mole%, lose their stability during OER process. Therefore, a minimum 20 mole% cobalt is needed for a high quality and efficient electrode before any modification, see Figure S13c (Supporting Information).

Since the electrodes with low cobalt (0–15%) are not stable under tough CP conditions and the $m\text{-LiMn}_{1.6}\text{Co}_{0.4}\text{O}_4$ and $m\text{-LiMn}_{1.5}\text{Co}_{0.5}\text{O}_4$ electrodes have good OER performance and stability, these electrodes were further modified by using SILAR-AN method. Therefore, the $m\text{-LiMn}_{1.6}\text{Co}_{0.4}\text{O}_4$ electrode with a lower cobalt content was chosen as a composition for further modification. Note also that the $m\text{-LiMn}_{1.7}\text{Co}_{0.3}\text{O}_4$ electrode has a good performance in OER process, but it is unstable during long CP experiments. Therefore, the $m\text{-LiMn}_{1.7}\text{Co}_{0.3}\text{O}_4$ electrode was also chosen for further modification to improve its stability.

Since 7 times coatings produce surface contamination over the electrodes, the $m\text{-LiMn}_{1.6}\text{Co}_{0.4}\text{O}_4$ electrode was coated up to 5 times to prepare 3 more electrodes, namely $m\text{-LiMn}_{1.6}\text{Co}_{0.4}\text{O}_4\text{-1}$, $m\text{-LiMn}_{1.6}\text{Co}_{0.4}\text{O}_4\text{-3}$, and $m\text{-LiMn}_{1.6}\text{Co}_{0.4}\text{O}_4\text{-5}$ and their CVs and long-term CP experiments (1 and 10 mA cm^{-2} for 12 and 6 h, respectively) were conducted. The results of these experiments are tabulated in Table 2. Both Tafel slope and overpotential values at 1 and 10 mA cm^{-2} of the $m\text{-LiMn}_{1.6}\text{Co}_{0.4}\text{O}_4\text{-#}$ electrodes decrease with increasing the number of coating. By modification, the $m\text{-LiMn}_{1.6}\text{Co}_{0.4}\text{O}_4\text{-#}$ electrode surface became very active and each coating provided a decrease

in the Tafel slope (down to $52.6 \pm 4.6\text{ mV dec}^{-1}$) that is even better than the Tafel slope of $m\text{-LiMnCoO}_4$ electrode (64 mV dec^{-1}).^[17]

The modification of $m\text{-LiMn}_2\text{O}_4$ also improved the Tafel slope of $m\text{-LiMn}_2\text{O}_4\text{-1}$ electrode but in further coatings, there was no trend. However, the multiple coatings further improved the Tafel slope of the $m\text{-LiMn}_{1.6}\text{Co}_{0.4}\text{O}_4\text{-#}$ electrodes. The CP experiments also show that the overpotentials at 1 and 10 mA cm^{-2} current densities are quite low, 265 and 311 mV, respectively, in the modified $m\text{-LiMn}_{1.6}\text{Co}_{0.4}\text{O}_4\text{-#}$ electrodes. The $m\text{-LiMn}_{1.6}\text{Co}_{0.4}\text{O}_4\text{-3}$ electrode has recorded overpotentials of 265 and 546 mV (without IR compensation) at 1 and 10 mA cm^{-2} current densities, respectively. Table S2 (Supporting Information) compares our Tafel slopes and overpotential values with a set of metal oxides from the recent literature. These results are the best results obtained among the samples, tested in this work and close to IrO_2 -based benchmark electrodes.^[7]

The CP measurements were also carried to check the electrode stability by recording CVs after CP experiments, see Figure 6. The modified $m\text{-LiMn}_{1.6}\text{Co}_{0.4}\text{O}_4\text{-#}$ electrodes display better stability compared to $m\text{-LiMn}_{1.6}\text{Co}_{0.4}\text{O}_4$. Especially, the current density loss, in the 0.7–1.0 V range, is small in the $m\text{-LiMn}_{1.6}\text{Co}_{0.4}\text{O}_4\text{-1}$ and $m\text{-LiMn}_{1.6}\text{Co}_{0.4}\text{O}_4\text{-3}$ electrodes. Moreover, the CVs after CP experiments at 1 and 10 mA cm^{-2} current densities of the $m\text{-LiMn}_{1.6}\text{Co}_{0.4}\text{O}_4\text{-5}$ show almost no change compared to the first CV of the same electrode before the CP experiment, see Figure 6b,c. Both, the targeted efficiency and stability have been achieved by modification in the $m\text{-LiMn}_{1.6}\text{Co}_{0.4}\text{O}_4\text{-#}$ electrodes.

To further reduce the cobalt content of the electrodes, we also tested the $m\text{-LiMn}_{1.7}\text{Co}_{0.3}\text{O}_4$ electrode that was at the border line between a stable and unstable electrode before modification. The $m\text{-LiMn}_{1.7}\text{Co}_{0.3}\text{O}_4\text{-1}$, $m\text{-LiMn}_{1.7}\text{Co}_{0.3}\text{O}_4\text{-3}$, and $m\text{-LiMn}_{1.7}\text{Co}_{0.3}\text{O}_4\text{-5}$ electrodes were prepared and tested by employing the same tests. The results of these tests are also tabulated in Table 2. The $m\text{-LiMn}_{1.7}\text{Co}_{0.3}\text{O}_4\text{-1}$ and $m\text{-LiMn}_{1.7}\text{Co}_{0.3}\text{O}_4\text{-3}$ electrodes also lose their stability to some extent during CP experiment, but $m\text{-LiMn}_{1.7}\text{Co}_{0.3}\text{O}_4\text{-5}$ electrode shows no current lost in the OER range. The CVs, after CP at 10 mA cm^{-2} , show that the current density lost is more in the $m\text{-LiMn}_{1.7}\text{Co}_{0.3}\text{O}_4\text{-1}$ electrode, but less significant in the $m\text{-LiMn}_{1.7}\text{Co}_{0.3}\text{O}_4\text{-3}$ electrode. It means that the modification is also successful in terms of stability of the $m\text{-LiMn}_{1.7}\text{Co}_{0.3}\text{O}_4$ electrodes. The slope of current density versus potential plot of the $m\text{-LiMn}_{1.7}\text{Co}_{0.3}\text{O}_4\text{-5}$ electrode is almost the same in the first (before CP) and last (after CP) CV curves (see Figure S14, Supporting Information),

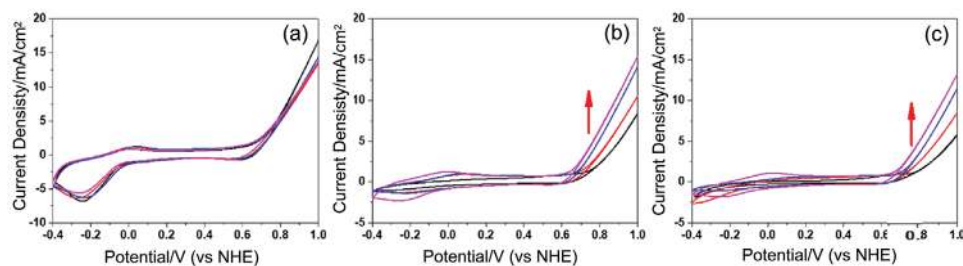


Figure 6. CVs of $m\text{-LiMn}_{1.6}\text{Co}_{0.4}\text{O}_4\text{-#}$ (# is 0, 1, 3, and 5) a) 1st set before CP, b) after 12 h CP at 1 mA cm^{-2} , and c) after 12 h at 1 mA cm^{-2} and 6 h at 10 mA cm^{-2} .

indicating that the $m\text{-LiMn}_{1.7}\text{Co}_{0.3}\text{O}_{4-5}$ electrode is as stable as the $m\text{-LiMn}_{1.6}\text{Co}_{0.4}\text{O}_{4\#}$ electrodes under our reaction conditions in long-runs.

2.3. Synergistic Effects Between the Mn and Co Sides in Electrocatalytic Mechanism of OER

The improved overpotential and faster kinetics of the water oxidation reaction could be related to an electronic synergy between Mn(III) and Co(III) species as suggested in O_2 reduction process over a mixed manganese and cobalt oxide using in situ XANES (X-ray absorption near edge structure) data by Wang et al.^[47,48] Accordingly, their reaction mechanism has been modified and improved for OER, as shown in Figure 7. To start with, surface species were neutral with 3 lattice oxygens, 2 water, and a hydroxide group at the surface in both metal ions to have a charge balance at the surface. Metal oxo ($\text{M}=\text{O}$) bond is also crucial for the $\text{O}-\text{O}$ bond formation in both commonly proposed two reaction mechanisms (nucleophilic acid-base, NAB, and radical coupling, RC, reactions) for both OER and O_2 reduction reactions.^[47-52] The NAB mechanism considers a nucleophilic acid-base reaction between metal oxo surface species and hydroxide ion. The other mechanism considers a radical coupling reaction between the $\text{M}=\text{O}$ species for the $\text{O}-\text{O}$ bond formation.^[47-52]

We believe that a nucleophilic path is active over our electrode surface, see latter. The water oxidation half-reaction is initiated by an internal redox reaction between the neighboring Mn(III) and Co(III) surface species that leads to an oxidation of the Mn(III)-OH and reduction of Co(III)-OH sites by abstracting a hydrogen from the Mn(III)-OH site. Since the

electronegativity of Mn is lower than Co (Millikan electronegativity of Mn is 3.72 eV and Co is 4.30 eV), the reaction in the first step produces a Co(II)-OH₂ and Mn(IV)=O sites and energetically favored. Notice also that the $(\text{O})_3\text{Mn(IV)=O}$ surface species has a C_{3v} point group and a d^3 electron configuration. The low-lying partially filled $e(d_{xz})$ and d_{yz} orbitals of Mn(IV) interact with the occupied oxygen $e(2p_x)$ and $2p_y$ orbitals to enhance the $\text{Mn}=\text{O}$ π -bond strength, see Figure S15 (Supporting Information). Therefore, the electron donation from oxygen to Mn(IV) through π -interaction improves the electrophilic character of the oxo-oxygen. Notice also that odd electron configuration (d^3) may also favor the RC mechanism.^[52] However, further electrochemical oxidation of Mn^{4+} to Mn^{5+} makes an even stronger electron donation from oxygen to manganese, due to a further increase in the electronegativity of Mn(V) side by oxidation that results a better π -interaction (better overlapping of the metal $e(d_{xz}, d_{yz})$ and oxygen $e(p_x)$ and p_y) orbitals due to reduced electronegativity difference) between Mn and O orbitals and produces a highly electrophilic oxo-oxygen for the nucleophilic attack by a hydroxide ion. Moreover, the formation of Mn^{5+} creates a positively charged side (Mn(V)=O^+) and attracts a hydroxide ion to its close vicinity for an effective nucleophilic reaction. The evidence for the formation of Mn^{5+} (with a d^2 configuration) species comes from the slow CV measurements of the $m\text{-LiMn}_2\text{O}_4$ and $m\text{-LiMn}_{2-x}\text{Co}_x\text{O}_4$ electrodes. The CVs at 2 mV s^{-1} scan rate displays a broad peak at around 0.0 V, due to delithiation of $m\text{-LiMn}_2\text{O}_4$ as already being previously discussed and another peak at around 0.30 V likely due to $\text{Mn}^{4+}/\text{Mn}^{5+}$ couple in an alkaline media, see Figure S16 (Supporting Information). Note also that the d^2 configuration favors the NAB path due to an amplified electrophilicity of the oxo-oxygen.^[52]

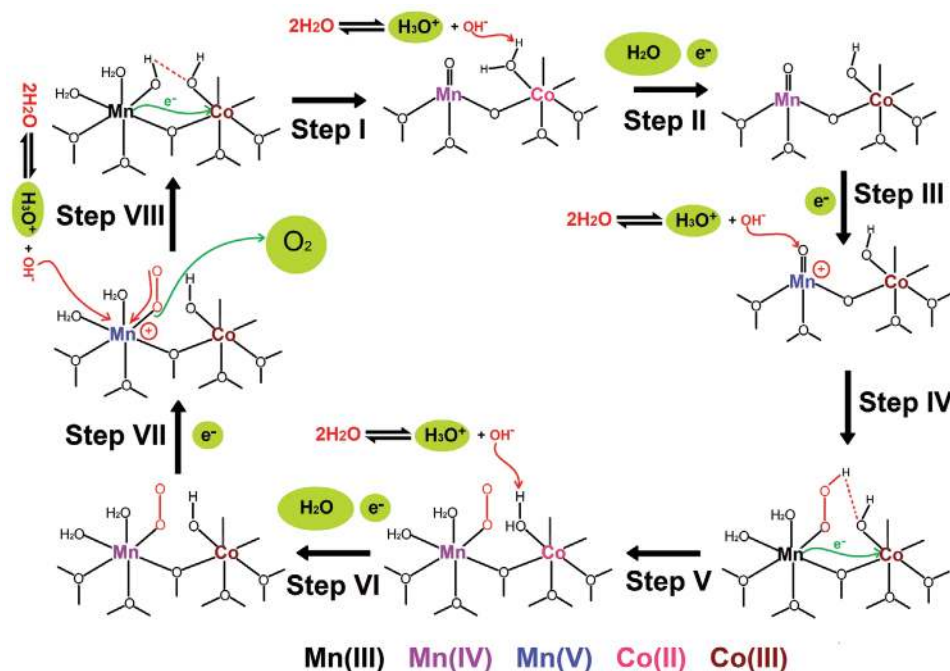


Figure 7. Schematic representation of a likely reaction mechanism during OER and representative surface species over the $m\text{-LiMn}_{2-x}\text{Co}_x\text{O}_4$ electrocatalyst.

Therefore, in the second step, the Co(II)–OH₂ side is electrochemically oxidized to produce the 1st electron and H⁺ ion (as H₃O⁺) of the 4 electrons and 4 H⁺ ions of the overall OER. In this step, a hydroxide ion captures a hydrogen from the coordinated water (Co(II)–OH₂ side) to produce a water molecule (or simply this could be an oxidative ligand exchange between a hydroxide ion in the solution and the coordinated water molecule). Note also that every hydroxide ion, used throughout the suggested mechanism, is a by-product of dissociation of 2 water molecules into a hydroxide (OH[−]) and hydronium (H₃O⁺) ions, therefore the mass and charge balances of the media are preserved throughout the process. The oxidative attack of the hydroxide in this step produces a H₃O⁺ ion (from the dissociation of water), H₂O, and an electron, see Figure 7. The third step of the process is another electrochemical oxidation process, where the Mn(IV)=O side is oxidized to Mn(V)=O⁺ by releasing the 2nd electron. This step also produces a Mn(V)=O⁺OH[−] side, where a hydroxide ion is in close vicinity to the Mn(V)=O⁺ side for an effective nucleophilic attack to form a peroxide (Mn(III)–O–O–H) specie, O–O bond formation, in the fourth step. Moreover, the formation of Mn–OOH releases 2 electrons (due to reduction of oxo and hydroxy oxygens (O^{2−}) to peroxide (O₂^{2−})) to Mn(V) to reduce it back to Mn(III) in step 4, see Figure 7. This step is the rate-determining step.^[52] However, further detailed analysis of each step needs to be investigated to determine the rate-determining step, which is critical for designing electrocatalysts. The fifth step proceeds by a reductive capture of peroxy-hydrogen by the neighboring Co(III)–OH side and regeneration of the Co(II)–OH₂ side and production of the Mn(IV)–O–O side (this is also energetically favored if the electronegativity is considered). Step 2 repeats in step 6 and produces Co(III)–OH back with the 3rd electron, H₃O⁺, and water. The last electron of the cycle is electrochemically produced by the oxidation of Mn(IV)–O–O to Mn(V)–O–O⁺/OH[−] in step 7. The last step of the process is; two electrons oxidative release of O₂ by an attack of a hydroxide ion in the close vicinity of Mn(V)–O–O⁺ side and reduction of Mn(V) back to Mn(III)–OH. This step also produces another H₃O⁺ ion and the electrocatalytic-cycle are complete, see Figure 7. The hydronium ions, which are needed in the other half-reaction (reduction of H⁺ to H₂) on the cathode side are produced in steps 2, 4, 6, and 8 by the dissociation of water in the media, where the hydroxide ion is needed in the OER. The overall reaction of the proposed

8 steps uses 2 water molecules (8 H₂O is used but 2 are reproduced in step 2 and 6 and 4 are reproduced as H₃O⁺ in steps 2, 4, 6, and 8) to produce an O₂ molecule, 4H⁺ ions (as H₃O⁺), and 4 electrons.

The reaction mechanism given above is suggested based on the electroneutrality principle, the electronegativity of the species, and experimental pieces of evidence. However, further mechanistic investigations are necessary to fully understand the reaction mechanism and the order of these steps and their rates. An appreciable electronegativity difference (0.58 eV) between Mn and Co improves the slow rate-determining step(s) (such as 1st and 4th steps, the formation of oxo side and nucleophilic attack of hydroxide ion to form Mn=O and Mn–OOH sides) and also high affinity of water (as evidenced from density functional theory (DFT) calculations^[48]) to Co side synergistically amplify the OER reaction. Our XPS data also support this proposal, such that increasing Co by SILAR-AN increases the intensity of O 1s peak of coordinated/adsorbed water, hydroxide, and peroxy/oxo species on the pore-walls. **Figure 8** shows a series of spectra before and after long-term CP experiments. The O 1s XPS spectra of the electrode after CV, chronoamperometry (CA), and long-run CP experiments display amplified peroxy or oxo peaks located at around 531.2 eV, see Figures S4 and 8a (Supporting Information). The Co 2p region loses the satellite peak at 786 eV, the main ²P_{3/2} peak becomes sharper with a weak satellite peak at around 790 eV, indicating the conversion of Co(II) to Co(III) species at the electrode surface, see Figure 8b. Similarly, the peak assigned to Mn(II) species disappears from the Mn 2p spectra upon long-term CP experiment, see Figure 8c. The spectral changes and quantitative analysis after series of CV, CA, and CP experiments show that the surface Mn(II) species are dissolved into the electrolyte media.^[53] Note also that the dissolution of Mn(II) into media has also been observed in lithium-ion batteries, constructed using LiMn₂O₄ anode, due to disproportionation reaction of Mn(III) sides to Mn(IV) and Mn(II) sides.^[53] Therefore, the Mn/Co ratio over the electrode surface drops to a level detected by EDX and XPS of the grind samples after CP experiments. The likely origin of the poor stability of m-LiMn₂O₄ electrodes could be the disproportionation of Mn(III) to Mn(IV) and more soluble Mn(II) species (Mn(II) species will form in place of Co(II) species in the mechanism over the Mn-rich electrode surface) during OER. Furthermore, the suggested mechanism is consistent with the in situ attenuated total reflectance fourier transform infrared

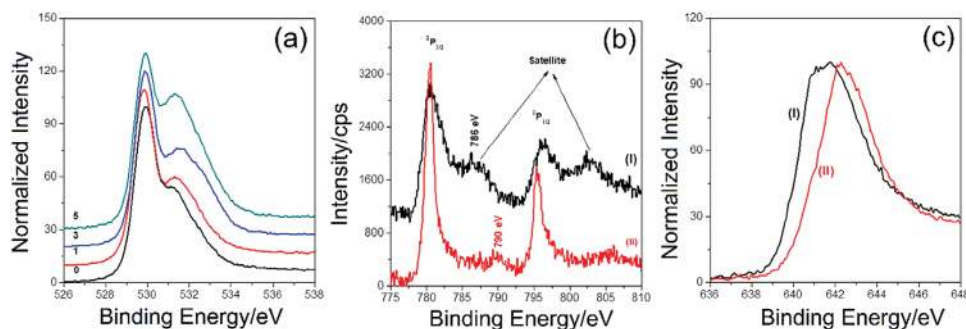


Figure 8. XPS spectra of electrode surface: a) O 1s region of m-LiMn₂O₄-# (# is 0, 1, 3, and 5 as marked on the spectra) after 12 h CP experiment at 1 mA cm^{−2}, b) Co 2p and c) Mn 2p (²P_{3/2}) regions of m-LiMn₂O₄-5 before (I) and after (II) CP experiment.

(ATR-FTIR) evidence, collected from cobalt oxide,^[54] iron oxide,^[55] and manganese oxide^[56,57] electrodes during and after OER process in various mechanistic studies in the literature. Presence of oxo-species (M(IV)=O), peroxides (M–OOH), and superoxide (O₂^{•-}) has been identified by in situ studies during the electrochemical process and later analysis of the used electrodes.^[54–57] However, further characterizations and kinetic studies, using surface sensitive in situ techniques and right (stable with a high surface area) electrodes, are required to fully understand the OER mechanism to design more efficient and stable electrocatalysts. Above proposed mechanism is an important attempt toward understanding OER over the metal oxides electrode surface and electronic synergic effects of two metals (Mn and Co) sites that collaboratively work together during OER on top surface of the m-LiMn_{2-x}Co_xO₄ electrodes.

3. Conclusion

MASA process is a one-pot synthesis method and applicable to synthesize mixed metal oxides (LiMn_{2-x}Co_xO₄, where x was varied from 0 to 0.5). A clear ethanol solution of all the ingredients (lithium, manganese, and cobalt salts and surfactants) can be spin or drop-cast coated over FTO-coated glass or bared glass as a lyotropic liquid crystalline gel thin or thick film. Then, the gel films are calcined to obtain mesoporous LiMn_{2-x}Co_xO₄ thin electrodes and powder samples, respectively, with high surface area. The m-LiMn_{2-x}Co_xO₄ electrodes can be further modified by employing SILAR-AN method to obtain m-LiMn_{2-x}Co_xO₄-# electrodes, in which the BET surface area and pore size gradually decrease with increasing the number of loading. The XPS, EDX, and XRD data collectively show that there is a Mn enrichment on the electrode outer surfaces in multiple SILAR-AN processes. Simply, the SILAR-AN method increases the cobalt content of the pore surface and the extracted Mn₃O₄ particles accumulate over the top surface of the electrodes.

The m-LiMn_{2-x}Co_xO₄ and m-LiMn_{2-x}Co_xO₄-# electrodes show good electrocatalytic performance OER in an alkaline media. The m-LiMn_{2-x}Co_xO₄ electrodes ($0 \leq x \leq 0.3$) are unstable for long-term OER, but the stability of the m-LiMn_{1.7}Co_{0.3}O₄ electrode can be improved by SILAR-AN modification. The modification reduces both Tafel slopes (as low as 46 mV dec⁻¹) and overpotential values (311 mV at 10 mA cm⁻²) of the electrodes. The MASA method is not sufficient by itself to obtain such low Tafel slopes from the m-LiMn_{2-x}Co_xO₄ electrodes, in which if the Co/Mn ratio is kept the same as in the active m-LiMn_{1.6}Co_{0.4}O₄-5 or m-LiMn_{1.7}Co_{0.3}O₄-5 electrodes. It is likely that the surface Co and Mn distribution over the electrode internal surface change with modification in a positive direction. Overall, the MASA and SILAR-AN methods need to be combined to produce stable and highly efficient m-LiMn_{2-x}Co_xO₄-# thin film electrodes with modest cobalt content.

The improved Tafel slope and low overpotential could be attributed to electronic synergy between the Mn and Co sites over the electrode surface. Higher electronegativity of Co over Mn is the driving force for the formation of Mn(IV)=O sites that can be further electrochemically oxidized to Mn(V)=O⁺ sites for an effective nucleophilic attack of hydroxide for the formation of peroxide and later for the release of oxygen during

the electrocatalytic process. Both Co and Mn sites synergistically (electronic effect) work together to produce 4 electrons needed for the overall water splitting. Two of these electrons are electrochemically produced by the oxidation of Mn sites and two from the oxidation of Co(II) sites that form during overall OER. The likely origin of decomposition of m-LiMn₂O₄ electrode is the disproportionation reaction of Mn(III) to Mn(IV) (active site) and Mn(II) (unstable site) that can be eliminated by incorporating Co into the m-LiMn_{2-x}Co_xO₄, where the disproportionation reaction produces rather stable and also active Co(II) sites in place of Mn(II). Note also that the Co(III)–Co(III) sites (in place of Mn(III)–Co(III)) are also stable and effective in the water oxidation process, however Mn(III)–Mn(III) sites are unstable and inefficient. The suggested mechanism also correlates well with the observed instability of LiMn₂O₄ in lithium ion batteries and OER process. The M(II) sites are particularly important in OER process and having a stable M(II) sites is a key for the OER process. The H⁺ ions are produced by the dissociation of water to hydronium and hydroxide ions that are used in the multistep water oxidation process.

The electrocatalytic path of OER is a multistep and 4-electron process that can be speeded up by appropriately designing materials with active sites and high surface area. Identifying the structure and composition of the active sites and/or species need further investigations by using in situ techniques to elucidate a more complete reaction mechanism for OER and to design more active and stable electrodes. Moreover, new investigations for improving stability of Mn(III) sites, using 1st row transition metals with high natural abundance, less toxicity, and high electronegativity are on the way using MASA and/or SILARAN to further improve the stability as well as performance of the electrodes.

4. Experimental Section

Synthesis of m-LiMn_{2-x}Co_xO₄ Thin Films: The method described in ref. [17] was used by only changing the composition of the initial clear solutions of the ingredients. Briefly, the clear homogeneous solutions were prepared by dissolving surfactants (P123 and CTAB) and salts (LiNO₃ and [M(H₂O)₆](NO₃)₂, where M is Mn(II) and Co(II)) in 5 mL ethanol, then they were acidified by adding 0.5 g concentrated nitric acid (70%) and stirred for overnight. The mole ratios of the ingredients in the solutions were 1:5:60 (P123:CTAB:salts). Only the Mn(II) and Co(II) mole ratios were varied from solution to solution by keeping the LiMn_{2-x}Co_xO₄ stoichiometry (x was varied from 0 to 0.5) as a reference. Table S3 (Supporting Information) tabulates the ingredient content of the solutions (solutions 1–6). Briefly, the solution 1 was prepared by dissolving first 0.173 g LiNO₃ in 5 mL ethanol, then 0.230 g CTAB, 0.719 g P123, 0.550 g HNO₃, and finally 1.255 g [Mn(H₂O)₆](NO₃)₂ (corresponds to 20:5:1:40, Li(I):CTAB:P123:Mn(II) mole ratio) were added to the above solution by stirring in an order with 5 min intervals and finally the overall solution was stirred overnight to obtain a clear solution for the preparation of mesoporous LiMn₂O₄. For the other compositions (LiMn_{2-x}Co_xO₄ (x is 0.1, 0.2, 0.3, 0.4, and 0.5)), solutions 2–6 were prepared only by reducing the amount Mn(II) salt and adding Co(II) salt in place in stoichiometric quantities. The amount of Mn(II) and Co(II) in the other 5 solutions (solutions 2–6) are 1.192 and 0.073 g, 1.130 and 0.145 g, 1.067 and 0.218 g, 1.004 and 0.291 g, 941 and 0.364 g, respectively. These solutions were spin or drop cast coated over FTO for the synthesis of electrodes or glass slides for bulk analysis (such as XRD pattern and N₂ adsorption–desorption isotherms), respectively. The spin or drop-cast coated films were directly calcined at 300 °C and annealed at higher temperatures for various purposes.

Modification of $m\text{-LiMn}_{2-x}\text{Co}_x\text{O}_4$ Electrodes: SILAR method was employed for the modification process. The $\text{LiMn}_{2-x}\text{Co}_x\text{O}_4$ films were coated with Co(II) species in three steps; in the 1st step, the film was dipped into a cobalt solution (1 M Co(II) solution, 14.547 g $[\text{Co}(\text{H}_2\text{O})_6](\text{NO}_3)_2$ dissolved in 50 mL deionized water) for 20 s, then in the 2nd step, it was removed from cobalt solution and hold over a paper towel (this ensures removing of any excess droplet over the film) and dipped into a deionized water bath for another 20 s, in the last step, step 2 was repeated using another deionized water bath to remove any undesired Co^{2+} species, accept a monolayer of Co^{2+} over the pore surface of the film. After monolayer coating, the film was calcined at 300 °C for 1 h and annealed at higher temperatures (such as 400 and 500 °C) for electrochemical analysis. Above process were repeated # many times to prepare mesoporous $\text{LiMn}_{2-x}\text{Co}_x\text{O}_4$ # (# is 1, 3, 5, and 7) electrodes.

Characterization: XRD patterns were collected using Rigaku Miniflex diffractometer, equipped with a Cu $K\alpha$ ($\lambda = 1.54056 \text{ \AA}$) X-rays source, operating at 30 kV 15 mA^{-1} and a Scintillator NaI(Tl) detector with a Be window and Pananalytical X'Pertpro Multipurpose X-ray diffractometer equipped with a Cu $K\alpha$ ($\lambda = 1.5405 \text{ \AA}$) X-rays source, operating at 45 kV 40 mA^{-1} . N_2 adsorption–desorption isotherms were collected using Micromeritics Tristar 3000 automated gas adsorption analyzer in the range of 0.01–0.99 P/Po. Around 150 mg sample was dehydrated under a vacuum of 35–40 mtorr at 200 °C for 2 h prior to measurement. Saturated pressure measurements were repeated every 120 min during a 6–10 h measurement. The SEM images were recorded using field electron and ion (FEI) Quanta 200 F scanning electron microscope on aluminum sample holders. The XPS spectra were collected using Thermo Scientific K-alpha X-ray photoelectron spectrometer operating with Al $K\alpha$ microfocused monochromatic source (1486.68 eV and 400 μm spot size) along with a flood gun for charge neutralization. The scraped powder samples from FTO electrodes were put on a copper tape for XPS analysis and the data were calibrated using C 1s peak. XPS spectra of the electrode surface were recorded by directly inserting the FTO-coated films into the spectrometer and making a contact between the electrode surface and spectrometer using a carbon type to avoid any surface charging. The electrochemical studies were carried out using $m\text{-LiMn}_{2-x}\text{Co}_x\text{O}_4$ # (x is 0, 0.1, 0.2, 0.3, 0.4, and 0.5 and # is 0, 1, 3, 5, and 7) coated FTO as working electrode, Pt wire as a counter electrode and Ag/AgCl (3.5 M KCl) electrode as a reference in a polypropylene cell with a 1.0 M KOH solution. The measurements were performed using a Gamry instrument (potentiostat-PC14G750). The measured potentials were corrected and reported to normal hydrogen electrode (NHE). Prior to electrochemical measurements, N_2 gas was purged into electrolyte solution for 15 min to get rid of any dissolved O_2 . CV, CA, and CP measurements were performed subsequently for each electrode. CVs of the $m\text{-LiMn}_{2-x}\text{Co}_x\text{O}_4$ # electrodes (working electrodes WEs) were recorded in the potential range of -0.4 – 1 V (vs NHE) with a scan rate of 50 mV s^{-1} . For each cyclic voltammogram, 3 cycles were collected, and the 2nd cycle was presented. Positive feedback method was not applied during the measurements; therefore, the data were reported without IR compensation. In the CA measurements, a predetermined potential was applied to the WEs to collect the current data. During the experiment, the electrolyte solution was stirred using a magnetic stirrer. At each potential, the potential was applied for 5–10 min, depending on how fast a stable current level was reached; the last current data point is reported and used in further analysis. Tafel slopes were determined with the help of chronoamperometry experiments. The starting potential for the OER is determined by 1st CV and earlier potential value is adjusted as a starting point for the CA experiment. Then the adjusted potential was applied to the WE by CA for 5–10 min and the current value at the end of experiment was reported. This step was repeated every 20 mV increments and the current values were recorded for each applied potential. Then, the applied overpotential versus $\log(j)$ was plotted and the linear region is fitted to evaluate the Tafel slopes. From the fits, a Tafel equation ($\eta = a + b \log(j)$, where η is overpotential (V), j is the current density (A cm^{-2}), a is an empirical value, and b is the Tafel slope (V dec^{-1})) is obtained to evaluate an estimated overpotentials at 1 and 10 mA cm^{-2} current densities. CP experiments were carried at constant current densities of

1 and 10 mA cm^{-2} to evaluate overpotential values of the WEs. Potential data were collected for 1–12 h, while stirring the electrolyte solution by a magnetic stirrer. The last data point was reported as a voltage value of the CP experiment. Then the potential required for OER (0.424 V vs NHE, from Nernst equation $E = E^0 - 0.0592 \cdot \text{pH}$, E^0 is 1.229 V and pH is 13.6) is subtracted from the collected data to evaluate the overpotential values.

Supporting Information

Supporting Information is available from the Wiley Online Library or from the author.

Acknowledgements

The authors thank to TÜBİTAK (under the Project No. 113Z730) for the financial support of this work. Ö.D. is a member of the Science Academy, Istanbul, Turkey.

Conflict of Interest

The authors declare no conflict of interest.

Keywords

lyotropic liquid crystals, molten salt assisted self-assembly, mesoporous thin films, SILAR, water oxidation electrocatalysts

Received: April 15, 2020

Revised: May 21, 2020

Published online: June 17, 2020

- [1] R. D. L. Smith, M. S. Prevot, R. D. Fagan, S. Trudel, C. P. Berlinguette, *J. Am. Chem. Soc.* **2013**, *135*, 11580.
- [2] L. Han, S. Dong, E. Wang, *Adv. Mater.* **2016**, *28*, 9266.
- [3] M. G. Walter, E. L. Warren, J. R. McKone, S. W. Boettcher, Q. Mi, E. A. Santori, N. S. Lewis, *Chem. Rev.* **2010**, *110*, 6446.
- [4] Y. Lee, S. Suntivich, K. J. May, E. E. Perry, Y. Shao-Horn, *J. Phys. Chem. Lett.* **2012**, *3*, 399.
- [5] Y. Zhao, E. A. Hernandez-Pagan, N. M. Vargas-Barbosa, J. L. Dysart, T. E. Mallouk, *J. Phys. Chem. Lett.* **2011**, *2*, 402.
- [6] C. C. L. McCrory, S. Jung, J. C. Peters, T. F. Jaramillo, *J. Am. Chem. Soc.* **2013**, *135*, 16977.
- [7] S. Jung, C. C. L. McCrory, I. M. Ferrer, J. C. Peters, T. F. Jaramillo, *J. Mater. Chem. A* **2016**, *4*, 3068.
- [8] T. Grewe, X. Deng, C. Weidenthaler, F. Schüth, H. Tüysüz, *Chem. Mater.* **2013**, *25*, 4926.
- [9] Y. Wang, T. Zhou, K. Jiang, P. Da, Z. Peng, J. Tang, B. Kong, W. Cai, Z. Yang, C. Zheng, *Adv. Energy Mater.* **2014**, *4*, 1400696.
- [10] L. Xu, Q. Jiang, Z. Xiao, X. Li, J. Hou, S. Wang, L. Dai, *Angew. Chem., Int. Ed.* **2016**, *55*, 5277.
- [11] T. Y. Ma, S. Dai, M. Jaroniec, S. Z. Qiao, *J. Am. Chem. Soc.* **2014**, *136*, 13925.
- [12] S. L. Brock, N. Duan, Z. R. Tian, O. Giraldo, H. Zhou, S. L. Suib, *Chem. Mater.* **1998**, *10*, 2619.
- [13] D. M. Robinson, Y. B. Go, M. Greenblatt, G. C. Dismukes, *J. Am. Chem. Soc.* **2010**, *132*, 11467.
- [14] C. Kuo, I. M. Mosa, A. S. Poyraz, S. Biswas, A. M. El-Sawy, W. Song, Z. Luo, S. Chen, J. F. Rusling, J. He, S. L. Suib, *ACS Catal.* **2015**, *5*, 1693.
- [15] C. Wei, Z. Feng, G. G. Scherer, J. Barber, Y. Shao-Horn, Z. J. Xu, *Adv. Mater.* **2017**, *29*, 1606800.

- [16] L. Köhler, M. E. Abishami, V. Roddatis, J. Ceppert, M. Risch, *ChemSusChem* **2017**, *10*, 4479.
- [17] F. M. Balci, I. Karakaya, E. P. Alsaç, M. Y. Yaman, G. Saat, F. Karadas, B. Ülgüt, Ö. Dag, *J. Mater. Chem. A* **2018**, *6*, 13925.
- [18] Y. Guo, J. Tang, H. Qian, Z. Wang, Y. Yamauchi, *Chem. Mater.* **2017**, *29*, 5566.
- [19] Y. Guo, J. Tang, Z. Wang, Y.-M. Kang, Y. Bando, Y. Yamauchi, *Nano Energy* **2018**, *47*, 494.
- [20] Y. Guo, T. Park, J. W. Yi, J. Henzie, J. Kim, Z. Wang, B. Jiang, Y. Bando, Y. Sugahara, J. Tang, Y. Yamauchi, *Adv. Mater.* **2019**, *31*, 1807134.
- [21] B. Tian, X. Liu, H. Yang, S. Xie, C. Yu, B. Tu, D. Zhao, *Adv. Mater.* **2003**, *15*, 1370.
- [22] A. Rumpleker, F. Kietz, E. Salabas, F. Schüth, *Chem. Mater.* **2007**, *19*, 485.
- [23] C. J. Brinker, Y. Lu, A. Sellinger, H. Fan, *Adv. Mater.* **1999**, *11*, 579.
- [24] G. Saat, F. M. Balci, E. P. Alsaç, F. Karadas, Ö. Dag, *Small* **2018**, *14*, 1701913.
- [25] A. Amirzhanova, I. Karakaya, C. B. Uzundal, G. Karaoğlu, F. Karadas, B. Ülgüt, Ö. Dag, *J. Mater. Chem. A* **2019**, *7*, 22012.
- [26] C. Karakaya, Y. Türker, C. Albayrak, Ö. Dag, *Chem. Mater.* **2011**, *23*, 3062.
- [27] C. Karakaya, Y. Türker, Ö. Dag, *Adv. Funct. Mater.* **2013**, *23*, 4002.
- [28] C. Avci, A. Aydınli, Z. Tuna, Z. Yavuz, Y. Yamauchi, N. Suzuki, Ö. Dag, *Chem. Mater.* **2014**, *26*, 6050.
- [29] Ö. Çelik, Ö. Dag, *Angew. Chem., Int. Ed.* **2001**, *40*, 3800.
- [30] C. Albayrak, N. Özkan, Ö. Dag, *Langmuir* **2011**, *27*, 870.
- [31] C. Albayrak, A. Cihaner, Ö. Dag, *Chem. – Eur. J.* **2012**, *18*, 4190.
- [32] H. M. Pathan, C. D. Lokhande, *Bull. Mater. Sci.* **2004**, *27*, 85.
- [33] M. A. Becker, J. G. Radich, B. A. Bunker, P. V. Kamat, *J. Phys. Chem. Lett.* **2014**, *5*, 1575.
- [34] T. Kannianen, S. Lindroos, T. Prohaska, G. Friedbacher, M. Leskela, M. Grasserbauer, L. Ninisto, *J. Mater. Chem.* **1995**, *5*, 985.
- [35] Z. Su, K. Sun, Z. Han, F. Liu, Y. Lai, J. Li, Y. Liu, *J. Mater. Chem.* **2012**, *22*, 16346.
- [36] I. Uzunok, J. Kim, T. O. Çolak, D. S. Kim, H. Kim, M. Kim, Y. Yamauchi, Ö. Dag, *ChemPlusChem* **2019**, *84*, 1544.
- [37] D. Tang, L. Ben, Y. Sun, B. Chen, Z. Yang, L. Gu, *J. Mater. Chem. A* **2014**, *2*, 14519.
- [38] H. W. Nesbitt, D. Banerjee, *Am. Mineral.* **1998**, *83*, 305.
- [39] S. Jeong, S. Park, J. Cho, *Adv. Energy Mater.* **2011**, *1*, 368.
- [40] J. C. Dupin, D. Gonbeau, P. Vinatier, A. Levasseur, *Phys. Chem. Chem. Phys.* **2000**, *2*, 1319.
- [41] M. C. Biesinger, B. P. Payne, A. P. Grosvenor, L. W. M. Lau, A. R. Gerson, R. St. C. Smart, *Appl. Surf. Sci.* **2011**, *257*, 2717.
- [42] M. M. Thackeray, P. J. Jonson, L. A. De Picciotto, W. I. F. David, P. J. Bruce, J. B. Goodenough, *Mater. Res. Bull.* **1984**, *19*, 179.
- [43] N. Li, C. J. Patrissi, G. Che, C. R. Martin, *J. Electrochem. Soc.* **2000**, *147*, 2044.
- [44] E. Hosono, T. Kudo, I. Honma, H. Matsuda, H. Zhou, *Nano Lett.* **2009**, *9*, 1045.
- [45] G. J. Wang, Q. T. Qu, B. Wang, Y. Shi, S. Tian, Y. P. Wu, R. Holze, *Electrochim. Acta* **2009**, *54*, 1199.
- [46] F. Cheng, Y. Su, J. Liang, Z. Tao, J. Chen, *Chem. Mater.* **2010**, *22*, 898.
- [47] Y. Yang, Y. Wang, Y. Xiong, X. Huang, L. Shen, R. Huang, H. Wang, J. P. Pastore, S. H. Yu, L. Xiao, J. D. Brock, L. Zhuang, H. D. Abruna, *J. Am. Chem. Soc.* **2019**, *141*, 1463.
- [48] Y. Wang, Y. Yang, S. Jia, X. Wang, K. Lyu, Y. Peng, H. Zheng, X. Wei, H. Ren, L. Xiao, J. Wang, D. A. Muller, H. D. Abruna, B. J. Wang, J. Lu, L. Zhuang, *Nat. Commun.* **2019**, *10*, 1506.
- [49] J. P. McEvoy, G. W. Brudvig, *Chem. Rev.* **2006**, *106*, 4455.
- [50] D. W. Shaffer, Y. Xie, J. J. Concepcion, *Chem. Soc. Rev.* **2017**, *46*, 6170.
- [51] W. Ruttinger, G. C. Dismukes, *Chem. Rev.* **1997**, *97*, 1.
- [52] T. A. Betley, Q. Wu, T. V. Voorhis, D. G. Nocera, *Inorg. Chem.* **2008**, *47*, 1849.
- [53] J. B. Goodenough, Y. Kim, *Chem. Mater.* **2010**, *22*, 587.
- [54] M. Zhang, M. Respinis, H. Frei, *Nat. Chem.* **2014**, *6*, 362.
- [55] O. Zandi, T. W. Hamann, *Nat. Chem.* **2016**, *8*, 778.
- [56] Z. N. Zahran, E. A. Mohamed, Y. Naruta, *ACS Catal.* **2016**, *6*, 4470.
- [57] K. Jin, H. Seo, T. Hayashi, M. Balamurugan, D. Jeong, Y. K. Go, J. S. Hong, K. H. Cho, H. Kakizaki, N. Bonnet-Mercier, M. G. Kim, S. H. Kim, R. Nakamura, K. T. Nam, *J. Am. Chem. Soc.* **2017**, *139*, 2277.